

1 **Quantifying above-cloud aerosol using spaceborne lidar for**
2 **improved understanding of cloudy-sky direct climate forcing**

3

4

5 **D. Chand^{*1}, T. L. Anderson¹, R. Wood¹, R. J. Charlson¹, Y. Hu², Z. Liu³, M.**
6 **Vaughan²**

7

8 1. Atmospheric Science Department, University of Washington, Seattle, WA, USA.

9 2. NASA Langley Research Center, Hampton, VA, USA.

10 3. Center for Atmospheric Sciences, Hampton University, Hampton, VA, USA.

11

12

13 * Corresponding author (duli@atmos.washington.edu Fax: +1 206 685 9302)

14

15

16

17 AGU Index Terms: 0305, 0321, 0360, 1640

18 Short Title: Quantify aerosol optical depth

1 **Abstract**

2 Estimates of global-mean direct climate forcing by absorbing aerosols located above
3 boundary layer clouds are large, uncertain, and almost entirely unconstrained by observations.
4 Spaceborne lidar offers a new opportunity for global constraints. Here we examine techniques
5 for using liquid water clouds as lidar targets, allowing aerosol optical depth and Ångström
6 exponent to be deduced directly from aerosol effects on light transmission. Two such techniques
7 are examined using data from the Cloud-Aerosol Lidar and Infrared Pathfinder Satellite
8 Observations (CALIPSO). The first is a previously reported method based on measurements of
9 cloud depolarization ratio (DR) at 532 nm wavelength. The second is a new method using
10 measurements of cloud color ratio (CR), which is the ratio of the signal from the cloud at 1064
11 nm to that at 532 nm. Optical depth retrievals from these two methods compare favorably over
12 the eastern tropical Atlantic Ocean during August, 2006, when biomass burning aerosols are
13 frequently advected over marine stratiform clouds. The CR technique is mainly sensitive to fine-
14 mode aerosols and essentially insensitive to clouds and coarse-mode dust. Because
15 anthropogenic aerosol is predominantly found in the fine mode, the CR technique can be used to
16 help identify situations where anthropogenic cloudy-sky direct radiative forcing is occurring. We
17 demonstrate this capability using six months data from the eastern tropical Atlantic Ocean.

1 1. Introduction

2 Following the usage in recent review articles (e.g. *Yu et al.* [2005]), we define direct
3 climate forcing (DCF) as the change in radiative flux at the top-of-atmosphere caused by
4 anthropogenic aerosols when considering only the direct interactions between radiation and
5 aerosol particles. (Indirect forcing involves aerosol-induced changes in clouds and will not be
6 considered here.) DCF is dominated by interactions in the shortwave due to the typically small
7 sizes of atmospheric aerosol particles [*Haywood and Shine* 1997] and its global and regional
8 magnitude is poorly constrained [*IPCC* 2007, *Schultz et al.* 2006]. Historically, DCF has been
9 divided into clear-sky and cloudy-sky portions [e.g., *Boucher and Anderson*, 1995; *Haywood et*
10 *al.*, 1997]. Aerosol retrievals from ground-based radiometers and passive satellite sensors have
11 helped to constrain clear-sky DCF, as summarized by *Yu et al.* [2005]. These same sensors are
12 of limited use for constraining cloudy-sky DCF, and this paucity of empirical constraints is
13 reflected in the uncertainty of current estimates. A recent comparison of nine global models
14 [*Schulz et al.*, 2006] found no agreement even as to the sign of the cloudy-sky DCF, with global-
15 annual-mean values ranging from -0.16 to +0.34 W/m².

16 Whether the direct effect of aerosols causes heating or cooling of the Earth system
17 depends primarily on the aerosol backscatter coefficient, the aerosol absorption coefficient, and
18 the albedo of the underlying surface [*Charlson and Pilat*, 1969; *Ensor et al.*, 1971; *Chylek and*
19 *Coakley*, 1974]. Based on this understanding, *Haywood et al.* [1997] pointed out that the most
20 important cloudy-sky forcing mechanism is the warming effect of absorbing aerosols located
21 within or above highly reflective boundary layer clouds. This mechanism in turn, is most
22 prominently displayed (in those models that exhibit a positive cloudy-sky DCF) over the
23 Southeast Atlantic where light-absorbing aerosols from African biomass burning activities are
24 advected over marine stratiform clouds. A positive cloudy DCF in this region has been inferred
25 from airborne measurements of aerosol and cloud properties by *Keil and Haywood* [2003]. The
26 maximum effect occurs around 0-20°S, extending off the coast for 20° or more over the
27 Southeast Atlantic Ocean, downwind of the biomass burning areas. However, the calculations
28 by *Keil and Haywood* [2003] are sensitive to assumptions about aerosol optical thickness and the
29 albedo of the underlying cloud, both of which were set to the maximum values observed during
30 the campaign. The modeling study by *Schulz et al.* [2006] further emphasizes the uncertainty of
31 cloudy-sky DCF for this region. The various models show annual-mean cloudy-sky DCF values
32 in the Southeast Atlantic that range from slightly negative to greater than +5 W/m². Unraveling
33 these uncertainties will require accurate constraints not only on the optical thickness and
34 radiative properties of the advecting aerosol layers, but also on the radiative properties of the
35 underlying cloud and the extent to which the aerosol and cloud are actually superposed.

36 Active sensing by spaceborne lidar offers a new opportunity for developing empirical
37 constraints on cloudy-sky DCF. Lidar profiles of attenuated backscatter (e.g. Figure 1) provide
38 unambiguous evidence of aerosol layers located above boundary layer clouds and can be used to
39 quantify some aspects of the problem such as frequency of occurrence and vertical separation.
40 Here we examine two novel techniques for using the 3-channel lidar data from Cloud-Aerosol
41 Lidar and Infrared Pathfinder Satellite Observations (CALIPSO) to provide much stronger
42 constraints on above-cloud aerosols.

43 Both methods use the underlying cloud as a reflectivity target. Figure 2 illustrates the
44 distribution of low level clouds judged to be suitable cloud targets by our selection criteria
45 (Section 2.4) for two different 16-day periods. Evidently, such clouds are routinely detected by

1 CALIPSO over the entire subtropical and eastern tropical Atlantic Ocean. Thus low clouds over
2 this region provide ample targets for studying elevated aerosol layers.

3 The depolarization ratio (DR) technique uses polarization information to deduce the
4 optical depth of the overlying atmosphere, as described by *Hu et al.* [2007a]. The color ratio
5 (CR) technique, reported here for the first time, uses dual wavelength information to identify
6 fine-mode aerosols (i.e. aerosols that are likely to be anthropogenic in origin) and to provide an
7 alternate method of deducing optical depth. The goals of this study is to develop practical
8 methodologies for exploiting these promising new techniques and to examine their strengths and
9 limitations in order to facilitate their use in improved global quantification of cloudy-sky DCF.

10 11 **2. Methods**

12 **2.1 CALIOP basics**

13 The CALIPSO satellite was launched April 28, 2006 for a nominal three-year mission as
14 part of the A-Train constellation of satellites [*Stephens et al.*, 2002]. *Winker et al.* [2002]
15 provide a detailed description of the CALIPSO instruments and *Winker et al.* [2007] assess
16 instrument performance over the first year of operation.

17 The primary CALIPSO instrument is the Cloud-Aerosol Lidar with Orthogonal
18 Polarization (CALIOP). CALIOP's laser transmits linearly polarized light simultaneously at 532
19 nm and 1064 nm at a pulse rate of 20.16 Hz and its receiver measures backscatter intensity at
20 1064 nm and 532 nm, with the latter divided into two orthogonally polarized components, giving
21 a total of three channels. CALIOP observes both clouds and aerosols at high spatial resolution as
22 shown, for example, in Figure 1. Level-1 CALIOP data consist of calibrated, geolocated, vertical
23 profiles of total attenuated backscatter at 532 nm, β'_{532} , perpendicularly polarized attenuated
24 backscatter at 532 nm, $\beta'_{p,532}$, and total attenuated backscatter at 1064 nm, β'_{1064} . From the
25 surface to eight km, the vertical resolution is 30 m and the horizontal resolution is 1/3 km.
26 (More specifically, laser pulses with a footprint of ~ 70 m at sea level are spaced 333 m apart.)
27 The β'_{532} channel is calibrated by examining molecular scattering returns from the mid-
28 stratosphere, assumed to be particle-free, at night. The other two channels are calibrated with
29 respect to β'_{532} . Calibration of $\beta'_{p,532}$ uses an on-board depolarizer periodically inserted upstream
30 of the polarization beam splitter. Calibration of β'_{1064} uses returns from optically thick cirrus
31 clouds that are sufficiently high that the beam does not pass through aerosol layers above them.
32 Such cirrus are assumed to backscatter with equal efficiency at the two wavelengths in
33 accordance with surface lidar observations [*Beyerle et al.* 2001]. Data quality is considerably
34 better at night because there is no background noise from scattered solar radiation and because
35 the primary calibration of the β'_{532} channel is continually updated. Calibration accuracy of all
36 channels under all conditions is being assessed through ongoing validation activities including
37 this study (e.g. the CALIPSO-CloudSat Validation Experiment, CC-VEX, during July and
38 August 2006 [*McCubbin et al.*, 2006].)

39 Level-2 data files provide the location and properties of atmospheric "features", identified
40 at averaging scales corresponding to horizontal resolutions from 1/3 km to 80 km. A feature (or
41 layer) is identified as a detectable departure from the expected profile for pure molecular
42 backscattering (CALIPSO Level-2 Algorithm Theoretical Basis Document¹, NASA, henceforth
43 *ATBD*, 2007). In addition to vertical and horizontal location, CALIOP provides three
44 fundamental pieces of information for each identified layer, corresponding to the vertical

¹ Available at http://www-calipso.larc.nasa.gov/resources/project_documentation.php

1 integrals (over the layer) of each lidar channel. As discussed below, it is useful to express these
2 three basic measurements as layer-integrated values of β'_{532} , depolarization ratio, and color ratio
3 (see section 2.3 for definitions of these latter two quantities). In contrast to these directly
4 measured quantities, advanced products like layer optical depth require additional, often assumed
5 information and a retrieval algorithm. In order to introduce the retrieval methods discussed
6 herein, we now discuss two distinct approaches to the retrieval of optical depth.

7 8 **2.2 Optical depth by forward iteration vs transmission methods**

9 Layer optical depth, τ_{layer} , is a Level-2 CALIPSO product provided for each identified
10 feature.² The standard retrieval method is an iterative, forward calculation that requires
11 knowledge of the extinction-to-backscatter ratio, S , of the scattering material within the layer
12 [ATBD, 2007]. Because S is, in general, uncertain and because the standard retrieval is highly
13 sensitive to errors in S (see, e.g., Stephens et al., [2001]), a preferred retrieval method is to use a
14 target of known reflectivity on the under side of the layer. In that case, the signal from this target
15 is reduced in direct proportion to the two-way transmissivity of laser light through the
16 intervening atmosphere. Such "transmission" methods [Young, 1995] tend to be simpler and
17 more accurate, largely because they do not require knowledge of S . Unfortunately, suitable lidar
18 targets are hard to find. The only established technique uses "clear air" - that is, portions of the
19 lidar profile assumed to be free of particles. For spaceborne lidar, this requires that a region of
20 particle-free air can be identified beneath the aerosol or cloud layer to be analyzed - a fairly
21 unusual situation except for thin cirrus. Moreover, 180° backscattering by air molecules is rather
22 weak at the mid-visible CALIOP wavelength (532 nm) and is much too weak to be useful at the
23 near-infrared wavelength (1064 nm). Optical depths obtained by the clear-air transmission
24 method will be included among the CALIOP Level-2 data products and, when available, these
25 will provide a valuable comparison to optical depths obtained by the standard forward iteration.
26 However, these data are too sparse to be used for constructing regional climatologies of lower
27 tropospheric clouds or aerosols.

28 Thus, a transmission technique that used a bright and commonly available lidar target
29 would be extremely useful. This paper examines two possible ways of using horizontally
30 extensive liquid water clouds for this purpose. Such clouds are common in the boundary layer.
31 The annual mean global low cloud coverage is approximately 40% [e.g. Rossow and Schiffer,
32 1999] and these clouds provide an enormous lidar signal at both CALIOP wavelengths.
33 Moreover, successful application of such techniques would provide data of direct relevance to
34 the problem of cloudy-sky DCF.

35 36 **2.3 Transmission techniques using liquid water clouds**

37 We describe these techniques in terms of products available in the CALIOP Level-2 files.
38 As mentioned above, Level-2 products include the altitude range and three directly measured
39 quantities for each layer. These consist of three extensive properties, corresponding to the three
40 lidar channels. It is convenient to represent these as one extensive property and two ratios - that
41 is, (i) layer integrated attenuated backscatter at 532 nm, γ'_{532} , (ii) layer integrated attenuated
42 depolarization ratio at 532 nm, δ'_{532} , which is the ratio of the perpendicular to the parallel
43 components of γ'_{532} , and (iii) layer integrated attenuated color ratio, χ' , which is the ratio of
44 integrated attenuated backscatter at 1064 nm (γ'_{1064}) to 532 nm (γ'_{532}). The two ratios, δ'_{532} and

² Note, however, that retrievals of τ_{layer} are not provided in the version 1 data products used herein.

1 χ' , form the basis of the two retrieval techniques. Note that throughout this manuscript, and in
 2 accordance with the CALIPSO *ATBD*, primed quantities indicate that the property being
 3 considered has not been corrected for attenuation by any aerosol or cloud particles that might be
 4 present above the layer in question.

6 2.3.1 Depolarization ratio (DR) method

7 *Hu et al.* [2007a] showed that the values of γ'_{532} and δ'_{532} obtained for opaque water
 8 clouds can be used to deduce the optical depth ($\tau_{\text{top,DR}}$) of overlying aerosol and/or cloud layers.
 9 As an initial test, *Hu et al.* [2007a] examined a case of thin cirrus overlying thick, marine
 10 boundary layer stratus and showed that $\tau_{\text{top,DR}}$ retrievals were consistent with retrievals from the
 11 traditional transmission technique in which particle-free air beneath the cirrus was used as the
 12 lidar target. This section reviews the nomenclature and physics of the DR technique.

13 An “opaque” cloud or aerosol layer is one that fully attenuates the lidar beam. For
 14 Nd:YAG-based backscatter lidars similar to CALIOP, complete attenuation of the signal occurs
 15 at single-scattering optical depths of ~ 3 [*McGill et al.* 2002]. Boundary layer clouds frequently
 16 exceed this optical depth such that opaque, low-level clouds are common in the CALIPSO data
 17 set. Let γ'_{water} represent, γ'_{532} for an opaque liquid water cloud and let $\gamma'_{\text{water,unobstructed}}$ represent
 18 the theoretical value of γ'_{water} if it were viewed by CALIOP through an atmosphere with
 19 negligible non-molecular attenuation. (Level-2 layer products are corrected for clear-air
 20 molecular attenuation above the layer.) In addition, let $\gamma'_{\text{water,SS}}$ represent the theoretical, single-
 21 scattering value of γ'_{water} - that is, the value that would be measured by a lidar with an infinitely
 22 narrow field of view such that only 180° backscattered photons, and no multiply-scattered
 23 photons, were detected. The relationship between these quantities was deduced by *Platt et al.*
 24 [1999] as follows,

$$25 \gamma'_{\text{water,SS}} = \gamma'_{\text{water}} \eta_c \quad (1a)$$

$$26 \gamma'_{\text{water,SS,unobstructed}} = \gamma'_{\text{water,unobstructed}} \eta_c = (2S_c)^{-1} \quad (1b)$$

27 where $\eta_c (\leq 1)$ is the cloud multiple scatter factor (which depends upon both cloud properties and
 28 lidar field of view) and S_c is the cloud extinction-to-backscatter ratio.

29 For liquid water clouds with droplets smaller than about $50 \mu\text{m}$, S_c is well known and
 30 narrowly constrained to about 19 sr [*Pinnick et al.*, 1983; *O'Connor et al.*, 2004; *Hu et al.*, 2006]
 31 at a wavelength of 532 nm, and *O'Connor et al* [2004] show negligible differences between S_c at
 32 532 and 1064 nm. Recently, *Hu et al.* [2006; 2007b] used three-dimensional radiative transfer
 33 calculations to show that, for the geometry of a spaceborne lidar like CALIOP, the multiple
 34 scattering factor, η_c , is strongly related to the cloud depolarization ratio, δ'_{water} . This relationship
 35 can be approximated by,

$$36 \eta_c \approx \left(\frac{1 - \delta'_{\text{water}}}{1 + \delta'_{\text{water}}} \right)^2 \quad (2)$$

37 A required assumption of the DR method is that δ'_{water} is negligibly affected by whatever aerosol
 38 or thin cloud layers lie between the liquid water cloud and the lidar instrument. If so, then the
 39 CALIOP data provide a measurement of $\gamma'_{\text{water,SS}}$ (via Equations 1a and 2) which can be
 40 compared to either a theoretically or empirically determined value of $\gamma'_{\text{water,SS,unobstructed}}$ (via
 41 Equation 1b) in order to deduce the amount of attenuation caused by the intervening atmosphere.
 42 Making use of the Beer-Lambert law governing transmission of light through an attenuating
 43 medium, we have:

$$\frac{\gamma'_{\text{water,SS}}}{\gamma'_{\text{water,SS,unobstructed}}} = T^2 = \exp(-2\tau_{\text{top,DR}}) \quad (3)$$

where T^2 is the two-way transmittance of the non-molecular atmosphere above the cloud. Solving for optical depth gives,

$$\tau_{\text{top,DR}} = -\frac{1}{2} \ln \left(\frac{\gamma'_{\text{water,SS}}}{\gamma'_{\text{water,SS,unobstructed}}} \right) \quad (4)$$

Rearranging terms, we can express the DR formula for above-cloud optical depth (at 532 nm) in terms of CALIOP Level-2 products as follows,

$$\tau_{\text{top,DR}} = -\frac{1}{2} \ln \left(\frac{\gamma'_{\text{water}}}{\gamma'_{\text{water,SS,unobstructed}}} \left(\frac{1 - \delta'_{\text{water}}}{1 + \delta'_{\text{water}}} \right)^2 \right) \quad (5a)$$

$$= -\frac{1}{2} \ln \left(2S_c \gamma'_{\text{water}} \left(\frac{1 - \delta'_{\text{water}}}{1 + \delta'_{\text{water}}} \right)^2 \right) \quad (5b)$$

Note that $\gamma'_{\text{water,SS,unobstructed}}$ acts as a calibration constant for the DR method. The theoretical or expected value of this constant, as shown by Equations (1b) and (5b), is $(2S_c)^{-1}$, or 0.026 sr^{-1} if we set S_c to its observed value of 19 sr (see Table 1). Using this value to retrieve $\tau_{\text{top,DR}}$, as in Equation (5b), relies on (i) the physical accuracy of the Platt relationship (Eqn 1b) and of the assumed value of S_c , (ii) the accuracy of the lidar calibration at 532 nm (both the parallel and perpendicular channels), and (iii) the accurate correction for molecular attenuation above the cloud in the Level-2 cloud layer products. Alternately, $\gamma'_{\text{water,SS,unobstructed}}$ can be determined empirically, as described in Section 2.5.2, by assembling data from opaque, liquid water clouds with no overlying clouds or aerosols.

2.3.2 Color ratio (CR) method

We introduce a new method for identifying and quantifying fine-mode aerosol layers overlying liquid water clouds. Because it uses data on the attenuated color ratio, χ' , we dub this the CR method. In this section we present the nomenclature and physical basis of this method.

The size distribution of aerosol mass in the atmosphere generally consists of two modes - a mechanically produced coarse mode and a fine mode produced by combustion and/or gas-to-particle conversion [Whitby *et al.*, 1972]. Over the visible to near-IR wavelength region, fine-mode aerosols exhibit optical extinction that is strongly wavelength dependent, whereas coarse-mode aerosols and cloud particles exhibit little or no wavelength dependence [van de Hulst, 1981]. To represent this optical behavior, we define an Ångström exponent [Ångström, 1929], \AA , in terms of the two CALIOP wavelengths, i.e.

$$\text{\AA} = \frac{-\ln \left(\frac{\tau_{1064}}{\tau_{532}} \right)}{\ln \left(\frac{1064}{532} \right)} \quad (6)$$

1 where τ_i represents optical depth at wavelength i . For fine-mode aerosols, which typically have
 2 volume equivalent diameters in the range 100-400 nm, \AA is in the range 1.5-3 (e.g. *Seinfeld and*
 3 *Pandis* [1998]).

4 Let χ'_{water} represent χ' for a liquid water cloud³ and let $\chi'_{\text{water,unobstructed}}$ represent the value
 5 of χ'_{water} if viewed by CALIOP through an atmosphere with negligible non-molecular
 6 attenuation. From the above discussion it follows that the presence of fine-mode aerosol
 7 overlying a cloud will cause stronger attenuation of the reflected laser light at 532 nm than at
 8 1064 nm which, in turn, will cause an increase in χ'_{water} . In contrast, thin clouds or coarse-mode
 9 aerosol above the cloud will cause little or no change in χ'_{water} . Therefore, χ'_{water} can be used to
 10 identify the presence of fine-mode aerosol above clouds.

11 The increase in χ'_{water} caused by overlying aerosol is a function of the aerosol optical
 12 depth and the aerosol Ångström exponent. For each of the two wavelengths, the signal from the
 13 cloud in terms of integrated attenuated backscatter, γ'_{water} , will be reduced by the two-way
 14 transmittance of the atmosphere (T_{532} and T_{1064} for the two CALIOP wavelengths). Therefore,
 15 invoking the Beer-Lambert law as in Eqn (3), we see that the observed cloud color ratio divided
 16 by the unobstructed cloud color ratio will be,

$$17 \quad \frac{\chi'_{\text{water}}}{\chi'_{\text{water,unobstructed}}} = \left(\frac{T_{1064}}{T_{532}} \right)^2 = \frac{\exp(-2\tau_{\text{top},1064})}{\exp(-2\tau_{\text{top},532})} \quad (7)$$

18 Solving for $\tau_{\text{top},532}$ and renaming this $\tau_{\text{top,CR}}$ for consistency with Equation (4) leads to the
 19 formula for overlying optical depth at 532 nm from the CR method:

$$20 \quad \tau_{\text{top,CR}} = \frac{1}{2} \ln \left(\frac{\chi'_{\text{water}}}{\chi'_{\text{water,unobstructed}}} \right) \frac{1}{(1 - 2^{-\text{\AA}})} \quad (8)$$

21 Just as $\gamma'_{\text{water,SS,unobstructed}}$ acts as a calibration constant for the DR method, $\chi'_{\text{water,unobstructed}}$ is a
 22 calibration constant for the CR method. The theoretical value of this constant is 1. Using this
 23 value to retrieve $\tau_{\text{top,CR}}$ relies on (i) the physical assumption that both 180° backscattering and
 24 multiple scattering exhibit no wavelength dependence for liquid water clouds, (ii) the accuracy of
 25 the lidar calibration (1064 nm calibration with respect to that at 532 nm), and (iii) the accurate
 26 correction for molecular attenuation above the cloud in the Level-2 cloud layer products.
 27 Alternately, these assumptions can be circumvented by determining $\chi'_{\text{water,unobstructed}}$ empirically,
 28 as described in Section 2.5.2.

30 2.3.3 Combination of the DR and CR method to estimate Ångström exponent

31 To recap, the DR method requires opaque target clouds, responds to a reduction in
 32 $\gamma'_{\text{water,SS}}$ compared to the value for unobstructed clouds, and retrieves above-cloud optical depth
 33 regardless of the nature of the overlying material. The CR method does not necessarily require
 34 opaque clouds, responds to an increase in χ'_{water} compared to the value for unobstructed clouds,
 35 and is primarily sensitivity to fine-mode aerosols.

36 To retrieve above-cloud optical depth, the CR method requires *a priori* knowledge of \AA .
 37 In situations where the aerosol type is well known (e.g. the African biomass burning cases
 38 considered here), \AA may be well constrained. In general, however, this is not the case, especially
 39 where the aerosol consists of an unknown mixture of fine and coarse components. Thus, it may
 40 be useful to combine the two techniques wherein the CR method identifies the presence of fine-

³ Note that the CR method does not necessarily require opaque clouds, as does the DR method.

1 mode aerosol, the DR method determines aerosol optical depth, and, using this as an input, the
 2 CR method determines the wavelength dependence of aerosol optical depth. Rearranging
 3 Equation (8), the expression for \hat{a} is,

$$4 \quad \hat{a} = -\frac{1}{\ln(2)} \ln \left(1 - \frac{1}{2\tau_{\text{top,DR}}} \ln \left[\frac{\chi'_{\text{water}}}{\chi'_{\text{water,unobstructed}}} \right] \right) \quad (9)$$

5 Section 3.2 describes application of Eqn. 9 for determination of the Ångström exponent using the
 6 combination of the DR and CR methods.

7 8 **2.4 Data selection**

9 Our analysis is based on daytime and nighttime CALIOP Level-2, Version 1, 5-km
 10 resolution cloud layer products over the eastern Atlantic Ocean (30°S-30°N, 40°W-40°E) during
 11 the six month period from June-November 2006. Version 1 is the first public release of Level-2
 12 data and does not yet contain advanced retrieval products such as aerosol or cloud optical depth.
 13 It does contain basic retrievals of layer top and bottom altitudes, vertical integrals of the three
 14 lidar channels, and layer categorization as either cloud or aerosol. We select lower tropospheric
 15 clouds (cloud top below 3 km) and confine our analysis to the Tropics in order to assure that all
 16 target clouds are composed of liquid water.

17 To investigate the properties of unobstructed cloud layers, we select a subset of the above
 18 data from a region (20-30°S, 0-10°E) and time (November 2006) when little or no overlying
 19 aerosol is expected, and we remove all cases in which the Level-2 data indicate overlying cloud
 20 layers. This "pristine" data subset is used to develop empirical estimates of the calibration
 21 constants - $\chi'_{\text{water,unobstructed}}$ and $\gamma'_{\text{water,SS,unobstructed}}$ - and their uncertainties, as described in Section
 22 2.5.2.

23 To compare the two methods of retrieving τ_{top} , we focus on a region (5-15°S, 0-10°E) and
 24 time (August, 2006) when maximum biomass burning aerosol was observed within our study
 25 area. According to *Klein and Hartmann [1993]*, mean low cloud cover for this region in August
 26 ranges from 60 to 75%. Results from this "polluted" data subset are presented in Section 3.1.

27 Implementing either the CR or DR method requires the identification of suitable cloud
 28 targets. Thin or patchy clouds, for example, would violate a basic assumption of the DR method
 29 and might cause problems for the CR method as well. These can be effectively identified and
 30 removed using Level-1 data; however, incorporating Level-1 data into our regional- and
 31 seasonal-scale analysis would require approximately 50 times the computational resources we
 32 have currently dedicated to this project. Therefore, we have developed screening criteria that use
 33 5-km Level-2 data only. Application of these criteria to unobstructed clouds (Section 2.5.2)
 34 allows us to evaluate their effectiveness. Screening criteria available in the Level-2 product files
 35 include the Cloud-Aerosol-Discrimination (CAD) Score and the reported uncertainties in the
 36 three basic layer properties: γ'_{water} , δ'_{water} , and χ'_{water} .

37 The CAD algorithm [*ATBD, 2007; Liu et al. 2004*] separates clouds and aerosols based
 38 on empirically determined, altitude-dependent histograms of their optical properties (backscatter
 39 intensity and its spectral dependence). If the observed properties of a layer fall in a region of
 40 parameter space where the histograms overlap, the more likely classification is selected and the
 41 CAD Score indicates the probability that the classification is correct. Many layers fall outside
 42 this overlap region and, thus, receive a CAD Score of magnitude 100 (complete confidence). In
 43 this study cloud layers are selected as reflectivity targets only when the reported CAD score is 90
 44 or higher. These target clouds are used to deduce overlying optical depth such that our method

1 does not involve the Level-2 aerosol layer products. Note that the CAD score in Version 1 is not
 2 necessarily an accurate confidence estimate since the histograms of cloud and aerosol properties
 3 are based on pre-launch data from airborne lidar. These are currently being revised in light of
 4 experience with actual CALIOP data.

5 Level-2 reported uncertainties in γ'_{water} , δ'_{water} , and χ'_{water} reflect random shot noise
 6 estimated for each 5-km retrieval block, as described by *Liu et al.* [2006]. We select target
 7 clouds only if the relative uncertainty in all three parameters is less than a threshold. For
 8 convenience, we define this threshold in terms of Signal-to-Noise (SNR) - the inverse of relative
 9 uncertainty. We find that the relative uncertainty of δ'_{water} is almost always the largest of the
 10 three such that the screening criterion primarily operates on this parameter. Results are highly
 11 sensitive to this threshold (see Sections 2.5.2 and 3.1), as will be shown by compare results for
 12 SNR thresholds of 2 (weak screening) and 5 (more strict screening).

14 2.5 Algorithm parameter estimation and uncertainties

15 Uncertainties are estimated using the standard method of propagation of errors:

$$16 \quad \delta F = \sqrt{\sum_{i=1}^n \left(\frac{\partial F}{\partial x_i} \delta x_i \right)^2} \quad (10)$$

17 where, F represents $\tau_{\text{top,DR}}$, $\tau_{\text{top,CR}}$ or \hat{a} derived from Eqns. (5), (8) and (9) respectively, x_i is the i^{th}
 18 independent variable of the function F , and n is the number of variables. In this study all
 19 uncertainties are given at the 1- σ level.

20 Each method of retrieving τ_{top} and its uncertainty requires knowledge of three parameters
 21 and their uncertainties. As shown in Table 1, these parameters divide into three categories:
 22 CALIOP Level-2 data, empirically determined calibration constants, and the Ångström
 23 exponent, \hat{a} , which appears in the CR method as an *a priori* constant. (The calibration constants
 24 can also be determined *a priori*; however, that is not our approach.) Reported uncertainties in
 25 Level-2 data involve random error and are discussed in Section 2.5.1. Uncertainties in
 26 calibration constants and \hat{a} involve systematic error and are discussed in Section 2.5.2.

28 2.5.1. Level-2 data and random error

29 The DR method (Equation 5) involves two Level-2 CALIOP variables γ'_{water} and δ'_{water}
 30 while the CR method involves just one, χ'_{water} . In all three cases, parameter uncertainties are
 31 provided in the data files. The reported uncertainties are calculated subsequent to averaging the
 32 15-shots within each 5-km retrieval block and, therefore, do not provide information on sub-5km
 33 variability. What they do provide are estimates of random, shot-noise error specific to each 5-
 34 km block [*Liu et al.*, 2006]. Because the source of uncertainty is random error, it can be reduced
 35 by further averaging.

36 To determine the random error in $\tau_{\text{top,DR}}$ we propagate uncertainties in γ'_{water} and δ'_{water}
 37 using Eqn. (10) applied to Eqn. (5a); similarly, to determine random error in $\tau_{\text{top,CR}}$, we propagate
 38 uncertainties in χ'_{water} using Eqn. (10) applied to Eqn. (8) For the month (August, 2006) and
 39 region (5-15° S, 0-10° E) of maximum biomass burning influence, the median random error in
 40 $\tau_{\text{top,DR}}$ is 0.08 during the night and 0.12 during the day. Uncertainties in both γ'_{water} and δ'_{water}
 41 contribute significantly to these errors but in general (and for both day and night) the error
 42 contribution from the polarization ratio δ'_{water} outweighs that from γ'_{water} by roughly a factor of
 43 two. For the same month and region, the median random error in $\tau_{\text{top,CR}}$ is 0.05 during the night

1 and 0.08 during the day. Thus, the random errors for the CR method are seen to be similar, but
2 smaller by a factor of about two-thirds. This reflects the common error source associated with
3 the 532 nm channel and the fact that the 1064 nm channel has much smaller random error than
4 the depolarization channel.

6 **2.5.2. Calibration constants and systematic error**

7 Unobstructed low clouds can be found on almost every orbit and are readily identified by
8 the CALIOP feature-finder. They offer an attractive approach to determining the calibration
9 constants required in the retrieval of τ_{top} for two reasons. First, this approach should largely
10 compensate for any errors in the calibration of the three CALIOP channels. Second, it provides
11 an empirical means of assessing the detection limit and the systematic error of the optical depth
12 retrievals.

13 To generate a large sample of unobstructed clouds, we select a month of data from a
14 remote $10^\circ \times 10^\circ$ region and we screen these data for the occurrence of high clouds. The resulting
15 statistics on the calibration constants for each method are shown in Table 2 and Figure 3. We
16 use this exercise as well to test the effect of two different noise-based screening criteria for target
17 clouds - a relatively weak criterion ($\text{SNR} > 2$, corresponding to relative error < 0.5) and a
18 stronger criterion ($\text{SNR} > 5$, or relative error < 0.2). (See Section 2.4 for further details.)

19 *Day versus Night:* Table 2 shows that the mean values of both calibration constants
20 differ substantially between day and night. These differences likely indicate uncorrected drift in
21 lidar calibration during the day associated with solar heating of the instrument. Improving the
22 daytime calibration of all three CALIOP channels is an ongoing priority for the CALIPSO
23 mission. For present purposes, we accept these differences as real and thereby apply separate
24 daytime and nighttime calibration constants to estimate τ_{top} .

25 *SNR test:* More stringent data screening ($\text{SNR} 5$ versus $\text{SNR} 2$) causes a 6% reduction of
26 sample number at night (from 1223 to 1155) and a 23% reduction during the day (from 645 to
27 498), indicating that the daytime data as a whole is much closer to the noise threshold. More
28 stringent screening does not cause a dramatic shift in the mean values of any of the calibration
29 constants, nor does it cause a substantial change in variability or detection limit for the CR
30 method. On the other hand, there is a dramatic effect on both variability and detection limit for
31 the DR method, especially during the day. The detection limit (DL) presented in Table 2 is the
32 minimum optical depth, τ_{top} , that can be detected with 99% confidence at 5-km resolution given
33 the observed variability for unobstructed clouds on the assumption that this variability is
34 normally distributed. (For the CR method, calculating DL requires an assumed value of $\hat{\alpha}$, which
35 was taken as 2.0.) More stringent screening causes a substantial reduction in the standard
36 deviation of $\gamma'_{\text{water,SS,unobstructed}}$ (DR method), which translates into a substantially lower DL.
37 Specifically, DL for $\tau_{\text{top,DR}}$ drops from 0.25 to 0.15 at night and from 0.31 to 0.11 during the day.

38 The DR method is much more sensitive to noise-based screening for two reasons. First,
39 the depolarization parameter, δ'_{water} , has the highest noise level (in a relative sense) of the three
40 parameters used in the retrievals. Second, high noise levels appear to be associated in many
41 cases with thin and/or patchy clouds. Such clouds, in turn, give approximately the same color
42 ratio as thick, continuous clouds but give a systematically lower value of $\gamma'_{\text{water,SS}}$. Note in Figure
43 3 that the DR distributions are strongly skewed to the left of the mean and that this tail is much
44 more pronounced for the lower SNR threshold. Thus, the effect on DR calibration of admitting
45 higher-noise samples is to cause a slight downward bias in the mean and a large increase in
46 variability, which, in turn, effects the detection limit. This issue of noise-based screening will be

1 discussed further in relation to the optical depth comparison (Figure 4 and Section 3.1). For
 2 now, we note that the DR method, when based on 5-km Level-2 CALIOP data as herein, could
 3 be substantially improved if there were Level-2 parameters that provided explicit information on
 4 sub-5-km cloud variability.

5 *DR versus CR:* As shown in Table 2, detection limits for the CR method are lower than
 6 for the DR method under all conditions and are much less affected by the choice of noise-based
 7 screening. In this sense, the CR method appears to be a more sensitive and robust retrieval
 8 technique. However, this statement applies only to the retrieval of fine-mode aerosol optical
 9 depth, since the CR method (unlike the DR method) has little or no sensitivity to coarse-mode
 10 aerosol or to overlying cloud layers.

11 *Ångström exponent:* The final issue concerning systematic error involves the value of \mathring{a}
 12 which must be assumed *a priori* in the retrieval of $\tau_{\text{top,CR}}$ (Eq. 8). Based on sunphotometer and
 13 in-situ measurements of biomass burning aerosols over Southern Africa and South America
 14 [Eck *et al.* 1999, 2001, 2003, Holben *et al.* 2001, Chand *et al.*, 2006], we assume a best-guess
 15 value of 2.0 with an uncertainty of ± 0.4 , as shown in Table 1. This assumption will be tested
 16 in two ways (see Section 3): by comparing optical depths derived from the DR and CR methods
 17 and by using the combined approach to estimate, rather than assume, \mathring{a} .

18 3. Results

19 3.1 Comparison of CR and DR aerosol optical depths

20 Figure 4 shows a comparison of $\tau_{\text{top,DR}}$ and $\tau_{\text{top,CR}}$ for the most polluted region (5-15°S,
 21 0-10°E) and month (August 2006) of our study domain. Error bars represent 1-sigma
 22 uncertainties, calculated as described in Section 2.5. For clarity, error bars are shown for every
 23 30th data point. The left and right panels on Figure 4 show nighttime and daytime data,
 24 respectively. The top and bottom panels show results for data screening at $\text{SNR} > 2$ and $\text{SNR} > 5$,
 25 respectively, as discussed in Sections 2.4 and 2.5.2. Data where either the DR or CR method
 26 indicates values below the detection limit (see Section 2.5.2 and Table 2) are not shown. The
 27 dashed lines show lines of constant Ångström exponent, which is a unique function of the ratio
 28 $\tau_{\text{top,CR}}/\tau_{\text{top,DR}}$ as seen by substitution of Eqn 8 for $\tau_{\text{top,CR}}$ into (9), i.e.

$$29 \quad \mathring{a} = -\frac{1}{\ln(2)} \ln \left(1 - \frac{3\tau_{\text{top,CR}}}{4\tau_{\text{top,DR}}} \right) \quad (11)$$

30 Figure 4 demonstrates substantial differences between the two methods in terms of the
 31 effects of data screening. When the weaker, $\text{SNR} > 2$ screening threshold is used (top panels), the
 32 detection limit for the DR method becomes quite high (around 0.3) such that a great many points
 33 at low optical depth are excluded. On the other hand, when the stronger, $\text{SNR} > 5$ screening
 34 threshold is used (bottom panels), nearly all the retrievals at high optical depth (greater than
 35 about 0.7) are excluded. This second observation is also attributable to the DR method, although
 36 it requires some explanation. Light attenuation associated with a thick, overlying aerosol layer
 37 causes a large reduction in the magnitude of γ'_{water} . As a result, the signal for the DR method
 38 becomes much smaller relative to the noise. With strong SNR screening, these high optical
 39 depth points are then excluded. The effect on the CR signal is much less pronounced.

40 In all four panels, most of the data points are located close to the line indicative of $\mathring{a} = 2$.
 41 This tends to justify our choice of $\mathring{a} = 2$ in the CR method and indicates good overall agreement
 42 for determining the optical depth of biomass burning aerosol. The upper panels, however, show
 43 a few cases where $\tau_{\text{top,DR}}$ is much higher than $\tau_{\text{top,CR}}$. There are two possible causes for these
 44 points. On the one hand, they could represent overlying layers exhibiting similar attenuation at

1 532 nm and 1064 nm - for example, optically thin cloud or dust particles. On the other hand, as
2 noted in Section 2.5.2, thin or broken target clouds tend to produce a positive artifact in the DR
3 method and the weaker screening threshold tends to accept more of this type of cloud target.
4 Thus, the outlier points in the top panels could also represent artificially amplified DR retrievals
5 associated with thin or broken clouds. A screening criterion based explicitly on sub-5-km
6 variability would likely resolve this problem, and a diagnostic parameter containing this
7 information would make a very useful addition to the set of Level-2 products.

8 Overall, the comparison shown in Figure 4 confirms previous suggestions that substantial
9 aerosol optical depths (i.e. greater than 0.3) occur quite commonly over marine stratiform clouds
10 off the coast of Southern Africa during the biomass burning season. Indeed, the CALIPSO
11 observations indicate that above-cloud aerosol optical depths in this region frequently exceed
12 0.6. In the next subsection we examine the geographical and seasonal distribution of such
13 elevated aerosol layers.

14 15 **3.2 Seasonal and geographical distribution of elevated aerosol layers**

16 Figure 5 displays the geographic distribution and optical thickness of optically thick fine-
17 mode aerosol layers ($\tau_{\text{top,CR}} > 0.3$) detected using the CR method over the entire eastern Atlantic
18 Ocean for each of the six months from June to November 2006. Keeping in mind that adjacent
19 orbit tracks are days or even weeks apart in time, these maps highlight the considerable temporal
20 variability in the optical properties at any location, underscoring the importance of
21 meteorological variability in determining the location and thickness of aerosol layers over the
22 ocean to the west of Southern Africa. Nevertheless, they show the seasonal cycle of Southern
23 African biomass burning [Ito *et al.*, 2007] in that there is a much greater prevalence of optically
24 thick, above-cloud aerosol layers during August and September than during other months. It is
25 also impressive that these layers can be seen to extend over 4000 km downstream of the source
26 regions. Detecting these extensive layers using clear-sky algorithms from passive satellite
27 sensors would be hampered by the persistent cloud cover in this region and by the difficulties
28 associated with screening out cloudy pixels.

29 Figure 6 shows the Ångström exponent, \AA , for each suitable CALIPSO overpass during
30 August 2006. The map indicates that $\text{\AA} = 2.0$ is a reasonable first approximation, especially for
31 the region of most intense biomass burning aerosol, but that lower Ångström exponents
32 (indicating larger particles) are found along an equatorial belt stretching across most of the
33 domain. The cause of this apparent geographical variation in Ångström exponent is not
34 presently known, but may be indicative of Saharan dust influence or cirrus clouds.

35 36 **4. Conclusions and Recommendations**

37 A new approach that uses *color ratio* (CR) from spaceborne lidar is applied to the
38 detection and characterization of aerosol layers overlying low clouds. The optical depth
39 retrievals from this approach are compared with a previous method (the *depolarization ratio*
40 method DR, Hu *et al.*, [2007a]), using CALIPSO Level-2 data off the coast of Southern Africa,
41 where biomass burning aerosols were frequently advected over marine stratiform clouds. Results
42 indicate good agreement within estimated uncertainties. The CR method is most sensitive to fine-
43 mode aerosols and essentially insensitive to thin clouds and coarse-mode dust. Because
44 anthropogenic aerosol is predominantly found in the fine mode, the CR method can be used to
45 identify situations where cloudy-sky anthropogenic forcing may be occurring. A combination of
46 the DR and CR methods is shown to yield important information on the aerosol size (Ångström

1 exponent). We demonstrate the capability of the CR method to detect elevated aerosol layers
2 associated with biomass burning using six months of data from the Southeast Atlantic. Layers
3 with aerosol optical depth greater than 0.3 are commonly observed up to several thousand
4 kilometers away from the source region over the Atlantic Ocean. The most geographically
5 extensive and highest aerosol optical depths are observed during August and September 2006,
6 with very few layers detected during November, 2006.

7 The prevalence and optical thickness of these aerosol layers above low marine boundary
8 layer clouds have important implications for the regional radiation budget over the subtropical
9 and tropical eastern Atlantic Ocean. Additionally, given that these aerosols are strongly
10 absorbing [Leahy *et al.* 2007] there are potentially important consequences for the atmospheric
11 heating rates and lower atmospheric stability which may impact the formation of low clouds.
12 Such layers present a challenge as they cannot be detected using conventional retrieval methods
13 such as those using surface-based sensors, or those using clear sky passive satellite retrievals.

14 Future studies are needed (1) to study how the calibration of the two methods vary with
15 season and latitude and for land vs ocean and (2) to combine these retrievals with MODIS-based
16 estimates of the underlying cloud albedo and *in-situ* derived single scattering albedo in order to
17 estimate the cloudy-sky DCF over the Southeast Atlantic. Such estimates ought to provide a
18 useful constraint for the evaluation of DCF in climate models.

19 Quantitative implementation of these retrieval methods based on Level 2, 5-km products
20 could be improved if the data files included information on horizontal homogeneity of the cloud
21 layer. For example, providing information on cloud fraction at 1 km and at single-shot
22 resolution would allow patchy clouds to be identified and eliminated. This, in turn, would
23 improve the ability to screen for suitable cloud targets, which is a problem in our current
24 approach, especially for the DR method.

25 We have demonstrated that both methods can be "self-calibrated" using observations
26 from unobstructed target clouds. Our analysis of one month of data from a remote oceanic
27 region found substantially different calibration constants during the daytime and nighttime. One
28 can anticipate that future implementations would benefit from studying orbit-to-orbit variations
29 in the calibration constants and even latitudinal variations within individual orbits. Such studies
30 should be possible given the prevalence of unobstructed low clouds around the globe and the
31 ability of the CALIOP feature-finder to identify these calibration targets.

32
33 **Acknowledgment** This work was supported by University of Washington startup funds, NASA's
34 CALIPSO Mission (contract NAS1-99105), the National Science Foundation (grants ATM-
35 0601177 and ATM-0205198), and the NASA Goddard Earth Sciences and Technology Program.

36

1 **References**

- 2 Ångström, A. (1929), On the atmospheric transmission of Sun radiation and on dust in the air,
3 Geogr. Ann., 11, 156 - 166.
- 4 Beyerle, G., M.R. Gross, D.A. Haner, N.T. Kjome, I.S. McDermid, T.J. McGee, J.M. Rosen, H.-
5 J. Schäfer, and O. Schrems (2001), A lidar and backscatter sonde measurement campaign at
6 Table Mountain during February-March 1997: Observations of cirrus clouds, *J. Atmos. Sci.*,
7 58, 1275-1287.
- 8 Boucher, O., and T.L. Anderson (1995), General circulation model assessment of the sensitivity
9 of direct climate forcing by anthropogenic sulfate aerosols to aerosol size and chemistry, *J.*
10 *Geophys. Res.*, 100, 26117-26134.
- 11 Chand, D., P. Guyon, P. Artaxo, O. Schmid, G. P. Frank, L. V. Rizzo, O. L Mayol-Bracero, L.
12 V. Gatti, and M. O. Andreae (2006) Optical and physical properties of aerosols in the
13 boundary layer and free troposphere over the Amazon Basin during the biomass burning
14 season, *Atmos. Chem. Phys.*, 6, 2911-2925.
- 15 Charlson, R.J., and M.J. Pilat (1969), Climate: the influence of aerosols, *J. Appl. Meteo.*, 8,
16 1001-1002.
- 17 Chylek, P., and J.A. Coakley (1974), Aerosols and climate, *Science*, 183, 75-77.
- 18 Eck, T., B. N. Holben, J. Reid, O. Dubovik, A. Smirnov, N. O'Neill, I. Slutsker, and S. Kinne
19 (1999), Wavelength dependence of the optical depth of biomass burning, urban, and desert
20 dust aerosols, *J. Geophys. Res.*, 104(D24), 31,333- 31,349.
- 21 Eck, T., et al. (2001), Characterization of the optical properties of biomass burning aerosols in
22 Zambia during the 1997 ZIBBEE field campaign, *J. Geophys. Res.*, 106(D4), 3425- 3448.
- 23 Eck, T., et al. (2003), Variability of biomass burning aerosol optical characteristics in southern
24 Africa during the SAFARI 2000 dry season campaign and a comparison of single scattering
25 albedo estimates from radiometric measurements, *J. Geophys. Res.*, 108(D13), 8477,
26 doi:10.1029/2002JD002321.
- 27 Ensor, D.S., W.M. Porch, M.J. Pilat, and R.J. Charlson (1971), Influence of the atmospheric
28 aerosol on albedo, *J. Appl. Meteo.*, 10, 1303-1306.
- 29 Haywood, J.M., D.L. Roberts, A. Slingo, J.M. Edwards, and K.P. Shine (1997), General
30 circulation model calculations of the direct radiative forcing by anthropogenic sulfate and
31 fossil-fuel soot aerosol, *J. Climate*, 10, 1562-1577.
- 32 Haywood, J. M., and K. P. Shine, 1997: Multi-spectral calculations of the direct radiative forcing
33 of tropospheric sulphate and soot aerosols using a column model. *Quart. J. Roy. Meteorol.*
34 *Soc.*, 123, 1907-1930.
- 35 Holben, B. N., D. Tanre, A. Smirnov, T. F. Eck, I. Slutsker, N. Abuhassan, W. W. Newcomb, J.
36 S. Schafer, B. Chatenet, F. Lavenu, Y. J. Kaufman, J. V. Castle, A. Setzer, B. Markham, D.
37 Clark, R. Frouin, R. Halthore, A. Karneli, N. T. O'Neill, C. Pietras, R. T. Pinker, K. Voss,
38 and G. Zibordi, 2001: An emerging ground-based aerosol climatology: Aerosol optical depth
39 from AERONET. *J. Geophys. Res.* 106, 12067-12097.

- 1 Hu, Y., Z. Liu, D. Winker, M. Vaughan, V. Noel, L. Bissonnette, G. Roy, and M. McGill (2006),
2 Simple relation between lidar multiple scattering and depolarization for water clouds, *Optics*
3 *Letters*, *31*, 1809-1811.
- 4 Hu, Y., M. Vaughan, Z. Liu, K. Powell, and S. Rodier (2007a), Retrieving optical depths and
5 lidar ratios for transparent layers above opaque water clouds from CALIPSO lidar
6 measurements, *Geosci. Rem. Sens. Lett.*, in press.
- 7 Hu, Y., M. Vaughan, Z. Liu, B. Lin, P. Yang, D. Flittner, W. Hunt, R. Kuehn, J. Huang, D. Wu,
8 S. Rodier, K. Powell, C. Trepte, and D. Winker (2007b), The depolarization - attenuated
9 backscatter relation: CALIPSO lidar measurements vs. theory, *Optics Express*, *15*, 5327-
10 5332.
- 11 Intergovernmental Panel of Climate Change (IPCC), *Climate Change 2007 - The Physical*
12 *Science Basis*. Contribution of Working Group I to the Fourth Assessment Report of the
13 IPCC, Cambridge University Press, 2007.
- 14 Ito, A., A. Ito, and H. Akimoto, 2007: Seasonal and interannual variations in CO and BC
15 emissions from open biomass burning in Southern Africa during 1998-2005. *Global*
16 *Biogeochemical Cycles*, *21*, No. GB2011.
- 17 Keil, A., and J. M. Haywood, Solar radiative forcing by biomass burning aerosol particles during
18 SAFARI 2000: A case study based on measured aerosol and cloud properties, *J. Geophys.*
19 *Res.*, *108*(D13), 8467, doi:10.1029/2002JD002315, 2003.
- 20 Klein, S. A. and D. L. Hartmann: 1993, The seasonal cycle of low stratiform clouds. *J. Climate*,
21 *6*, 1588-1606.
- 22 Leahy, L. V., T. L. Anderson, T. F. Eck, and R. W. Bergstrom (2007), A synthesis of single
23 scattering albedo of biomass burning aerosol over southern Africa during SAFARI 2000,
24 *Geophys. Res. Lett.*, *34*, L12814, doi:10.1029/2007GL029697.
- 25 Liu, Z., M. A. Vaughan, D. M. Winker, C. A. Hostetler, L. R. Poole, D. Hlavka, W. Hart, and M.
26 McGill (2004), Use of probability distribution functions for discriminating between cloud
27 and aerosol in lidar backscatter data, *J. Geophys. Res.*, *109*, D15202,
28 doi:10.1029/2004JD004732.
- 29 Liu, Z., W. Hunt, M.A. Vaughan, C.A. Hostetler, M. McGill, K. Powell, D. Winker, and Y. Hu
30 (2006), Estimating random errors due to shot noise in backscatter lidar observations, *Appl.*
31 *Optics*, *45*, 4437-4447.
- 32 McCubbin, I. B., Trepte, C., Mace, J., Heymsfield, A., Marchand, R., Austin, R., Heymsfield, G.,
33 McGill, M., Myers, J., Pitts, M., Nguyen, L. (2006), "Overview of the Multi-Aircraft
34 CALIPSO-CloudSAT Validation Experiment" *Eos Trans. AGU*, *87*(52), Fall Meet. Suppl.,
35 Abstract A51E-0146.
- 36 McGill, M.J., D.L. Hlavka, W.D. Hart, V.S. Scott, J.D. Spinhirne, and B. Schmid (2002), "The
37 Cloud Physics Lidar: Instrument description and initial measurement results," *Appl. Optics*,
38 *41*, 3725-3734.
- 39 O'Connor, E.J., A.J. Illingworth, and R.J. Hogan (2004), A technique for autocalibration of cloud
40 lidar, *J. Atmos. Ocean. Tech.*, *21*, 777-786.

- 1 Pinnick, R.G., S.G. Jennings, P. Chylek, C. Ham, and W.T.J. Grandy (1983), Backscatter and
2 extinction in water clouds, *J. Geophys. Res.*, *88*, 6787-6796.
- 3 Platt, C.M.R., D.M. Winker, M.A. Vaughan, and S.D. Miller (1999), Backscatter to extinction
4 ratios in the top layers of tropical mesoscale convective systems and in isolated cirrus from
5 LITE observations, *J. Appl. Meteor.*, *38*, 1330-1345.
- 6 Rossow, W.B., and R.A. Schiffer, 1999: Advances in understanding clouds from ISCCP. *Bull.*
7 *Amer. Meteorol. Soc.*, *80*, 2261-2288.
- 8 Schulz, M., C. Textor, S. Kinne, Y. Balkanski, S. Bauer, T. Berntsen, T. Berglen, O. Boucher, F.
9 Dentener, S. Guibert, I.S.A. Isaksen, T. Iversen, D. Koch, A. Kirkevåg, X. Liu, V.
10 Montanaro, G. Myhre, J.E. Penner, G. Pitari, S. Reddy, Ø. Seland, P. Stier, and T. Takemura
11 (2006), Radiative forcing by aerosols as derived from the AeroCom present-day and pre-
12 industrial simulations, *Atmos. Chem. Phys.*, *6*, 5225-5246, 2006
- 13 Seinfeld, J. H, and S. N. Pandis, 1998: *Atmospheric Chemistry and Physics : From Air Pollution*
14 *to Climate Change*, Wiley-Interscience, New York.
- 15 Stephens, G.L., R.J. Engelen, M. Vaughan, and T.L. Anderson (2001), Toward retrieving
16 properties of the tenuous atmosphere using space-based lidar measurements, *J. Geophys.*
17 *Res.*, *106*, 28143-28157.
- 18 Stephens, G.L., D.G. Vane, R.J. Boain, G.G. Mace, K. Sassen, Z. Wang, A.J. Illingworth, E.J.
19 O'Conner, W.G. Rossow, S.L. Durden, S.D. Miller, R.T. Austin, A. Benedetti, and C.
20 Mitrescu (2002), The CloudSat mission and the A-Train, *Bull. Amer. Meteo. Soc.*, *83*, 1771-
21 1790.
- 22 Van de Hulst, H. C., 1981: *Light scattering by small particles*. Dover Publications, New York.
- 23 Winker, D. M., J. Pelon, and M. P. McCormick (2002), The CALIPSO mission: Spaceborne
24 lidar for observation of aerosols and clouds, *Proc. SPIE Int. Soc. Opt. Eng.*, *4893*, 1-11.
- 25 Winker, D., B. Hunt, and M. McGill (2007), Initial performance assessment of CALIOP,
26 *Geophys. Res. Lett.*, *submitted*, March 29, 2007.
- 27 Whitby, K.T., R.B. Husar, and Y.H. Liu (1972), The aerosol size distribution of Los Angeles
28 smog, *J. Colloid Interface Sci.*, *39*, 177-204.
- 29 Young, S.A. (1995), Analysis of lidar backscatter profiles in optically thin clouds, *Appl. Optics*,
30 *34*, 7019-7031.
- 31 Yu, H., Y.J. Kaufman, M. Chin, G. Feingold, L.A. Remer, T.L. Anderson, Y.J. Balkanski, O.
32 Boucher, S.A. Christopher, J. Feichter, R.A. Kahn, D. Koch, N.G. Loeb, M. Schulz, T.
33 Takemura, L. Zhou, and P. DeCola (2005), A review of measurement-based assessment of
34 aerosol direct radiative effect and forcing, *Atmos. Chem. Phys.*, *5*, 7647-7768.

1 **Table 1.** Data symbols, sources and uncertainties for parameters used to retrieve τ_{top} by both CR
 2 and DR methods.

3
 4

Method	Parameter	Source	Value and Uncertainty
DR Method	γ'_{water}	Level-2 data	variable
	δ'_{water}	Level-2 data	Variable
	$[\gamma'_{\text{water,SS,unobstructed}}]^1$	$[a\text{ priori}]^2$	$[0.026 \pm 0.0015]$
	$\gamma'_{\text{water,SS,unobstructed}}$	Empirical ³	see Table 2
DR Method	χ'_{water}	Level-2 data	Variable
	$[\chi'_{\text{water,unobstructed}}]^1$	$[a\text{ priori}]^4$	$[1.0 \pm 0.15]$
	$\chi'_{\text{water,unobstructed}}$	Empirical ³	see Table 2
	$[\text{\AA}]$	$[a\text{ priori}]$	$[2.0 \pm 0.4]$

5 ¹ Not used in this study, but included for completeness
 6 ² See Section 2.3.1
 7 ³ This work
 8 ⁴ See Section 2.3.2
 9

1 **Table 2** Key parameters in the DR and CR methods determined using unobstructed low clouds
2 (tops < 3 km) over a pristine region of the eastern Atlantic Ocean (30-20°S, 0-10°E) for the
3 month of November 2006. The calculations are made using signal to noise ratio (SNR=2, 5) of
4 unobstructed χ'_{water} , γ'_{water} and δ'_{water} . Means, percentiles (5th, 50th and 95th) and standard
5 deviations (SD) of the distributions of unobstructed attenuated backscatter $\gamma'_{\text{water,SS,unobstructed}}$ and
6 unobstructed color ratio $\chi'_{\text{water,unobstructed}}$ are given for day and night separately. Based upon the
7 distributions of unobstructed properties, a detection limit (DL) can be determined for the DR and
8 CR methods. The DL is the critical value of $\gamma'_{\text{water,SS}}$ or χ'_{water} for which we reject the hypothesis
9 (at the 99% level) that the air above the cloud contains no aerosol layer. The MDL is calculated
10 assuming normal statistics as $DL_{\text{DR}} = \bar{x} - 2.33\sigma$ (DR method) and $DL_{\text{CR}} = \bar{x} + 2.33\sigma$ (CR
11 method) where 2.33 represents the critical *t-value* for the respective degrees of freedom during
12 day and night ($N_{\text{day_SNR2}} = 645$; $N_{\text{night_SNR2}} = 1223$, $N_{\text{day_SNR5}} = 498$; $N_{\text{night_SNR5}} = 1155$). Thus, for
13 the DR method, if $\gamma'_{\text{water,SS}} < DL_{\text{DR}}$ we classify the cloud as having an elevated aerosol layer
14 above (for the CR method χ'_{water} must *exceed* DL_{CR}). The corresponding MD of AOD (τ) is also
15 given for both methods.
16

<i>Time</i>	$\gamma'_{\text{water_SS_unobstructed}}$			$\chi'_{\text{water_unobstructed}}$		
	Mean (5 th , 50 th , 95 th %)	SD	$DL_{\text{DR}} (\tau)$	Mean (5 th , 50 th , 95 th %)	SD	$DL_{\text{CR}} (\tau)$
SNR=2						
Day	0.019 (0.008, 0.02, 0.023)	0.004	0.009 (0.31)	1.2 (1.02, 1.20, 1.32)	0.09	1.40 (0.11)
Night	0.029 (0.016, 0.03, 0.034)	0.005	0.017 (0.25)	1.08 (0.99, 1.07, 1.20)	0.06	1.23 (0.08)
SNR=5						
Day	0.021 (0.018, 0.021, 0.023)	0.002	0.017 (0.11)	1.22 (1.13, 1.22, 1.32)	0.07	1.38 (0.08)
Night	0.030 (0.023, 0.030, 0.034)	0.003	0.022 (0.15)	1.08 (0.99, 1.07, 1.20)	0.06	1.22 (0.08)

17

18

19

1 **Figure Captions**

2 **Figure 1** CALIOP total attenuated backscattered signal at 532 nm (units $\text{sr}^{-1} \text{km}^{-1}$) observed from
3 01:17:53.3652 UTC to 01:31:12.3412 UTC on August 13th, 2006. Geographical locations of the
4 observation are shown by the altitude, latitude (Lat) and longitude (Lon). Strong backscattering
5 ($>0.001 \text{sr}^{-1} \text{km}^{-1}$) is associated with aerosol and/or cloud layers (as indicated by arrows). Low
6 level clouds (tops 1-1.5 km altitude) are covered by an extensive aerosol layer from
7 approximately 2-18°S. The aerosol layer extends up to almost 5 km altitude. Such a situation
8 occurs very frequently during the biomass burning season (particularly August and September)
9 over the west coast of Africa between the equator and 20°S.

10

11 **Figure 2** Map showing locations where CALIOP observes low level ($< 3 \text{ km}$) clouds as
12 determined by the Level-2 cloud mask (CAD score > 90 , SNR >2) for 1-16 August, 2006 (left)
13 and 16-30 November 2006 (right). The color indicates the height of the top of the cloud layers.
14 The CALIPSO repeat the ground track sampling approximately in 16 days so that the map serves
15 as a qualitative demonstration of the prevalence of low clouds over the eastern Atlantic Ocean.

16

17 **Figure 3** Histograms showing the distribution of $\gamma'_{\text{water,SS,unobstructed}}$ (panels a, c, e and g) and
18 $\chi'_{\text{water,unobstructed}}$ (panels b, d, f, and h) as determined using low cloud layers (tops $< 3 \text{ km}$)
19 unobstructed by cloud layers above 3 km in a relatively pristine region (20-30°S, 0-10°E) during
20 November 2006. The upper and lower four panels are for SNR >2 and SNR >5 , respectively.
21 Similarly, the left and right four panels are for night and day time, respectively. Layers with a
22 CAD score ≤ 90 are excluded (see text). For more details and a statistical summary of these
23 distributions see Table 1 and Table 2.

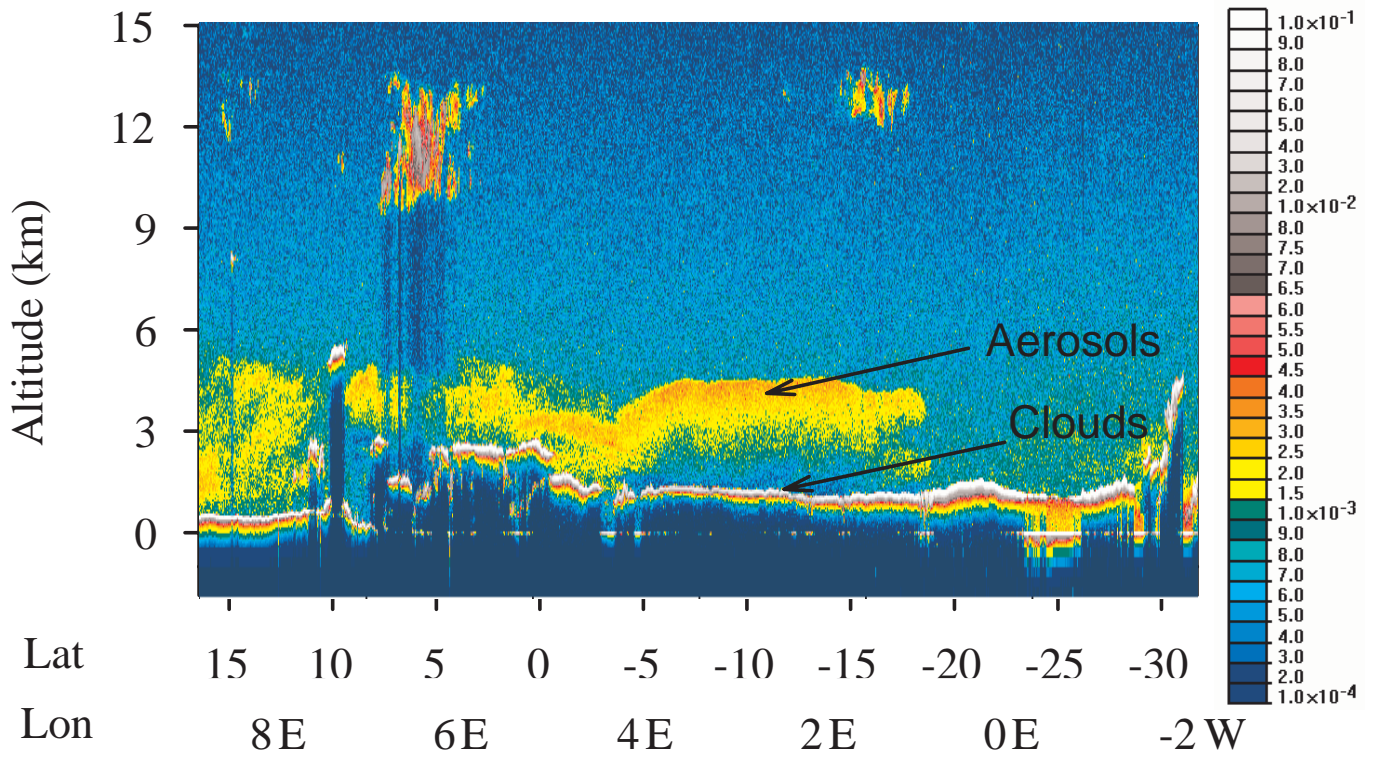
1 **Figure 4** Comparison of aerosol optical thickness calculated using CR method ($\tau_{top,CR}$) with that
2 from the DR method ($\tau_{top,DR}$) for nighttime (left) and daytime (right) CALIOP observations for
3 the region 5-15°S, 0-10°E during August 2006. Using the signal to noise ratio (SNR) of
4 unobstructed χ'_{water} , γ'_{water} and δ'_{water} , the top two and bottom two panels are made when $SNR > 2$
5 and $SNR > 5$, respectively. The error bars show the 1- σ uncertainties for the respective methods,
6 which for clarity reasons are plotted only for a randomly-selected 3% of the data points. Data
7 where either the DR or CR method indicates values below the detection limit (see Sections 2.5.1
8 and 2.5.2) are not shown. The dashed lines show the Ångström exponent α from Eqn. 11.

9
10 **Figure 5:** Maps showing the geographical distribution and optical thickness (colors) $\tau_{top,CR}$ of
11 optically thick ($\tau_{top,CR} > 0.3$) aerosol layers overlying clouds from the CR method for the months
12 of June-November 2006. All available day and night time data ($CAD > 90$, $SNR > 2$) are used as
13 per Table 2.

14
15 **Figure 6:** Map showing the Ångström exponent α (colors), derived using Eqn. 9, of elevated
16 aerosol layers above low clouds during August, 2006. Both day and night time data are used in
17 this plot. The box shows the area with highest $\tau_{top,CR}$ and α just downwind of the major biomass
18 burning region.

19

1 **Figure 1**

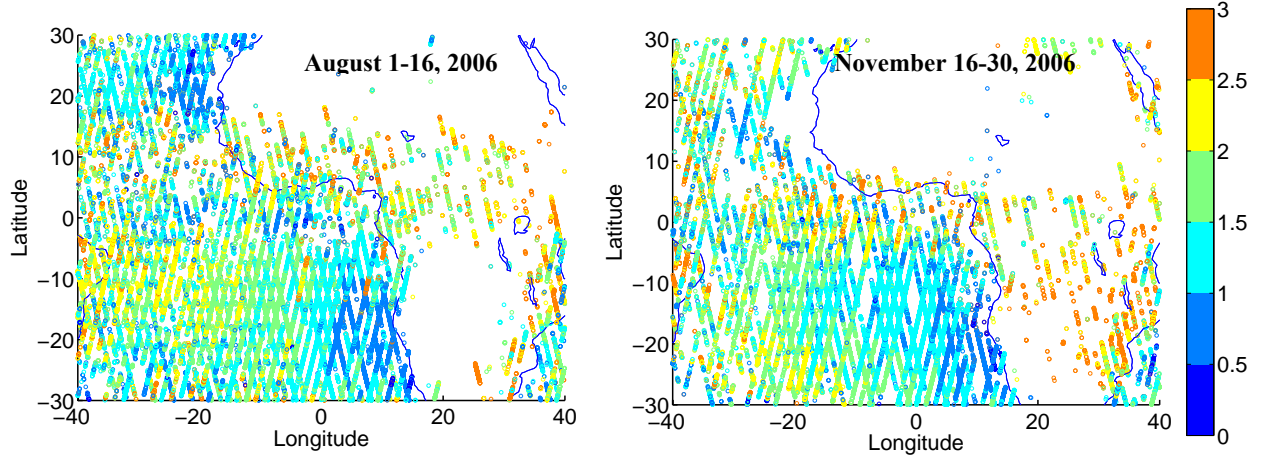


2

3

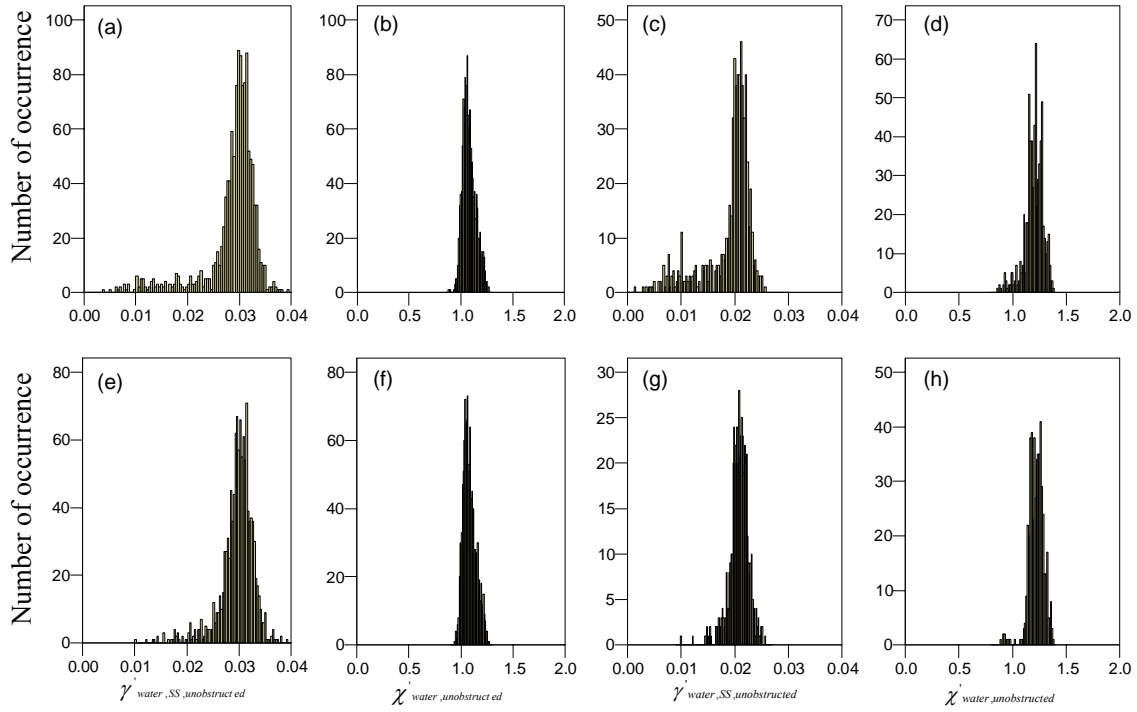
1 **Figure 2**

2



1 **Figure 3**

2

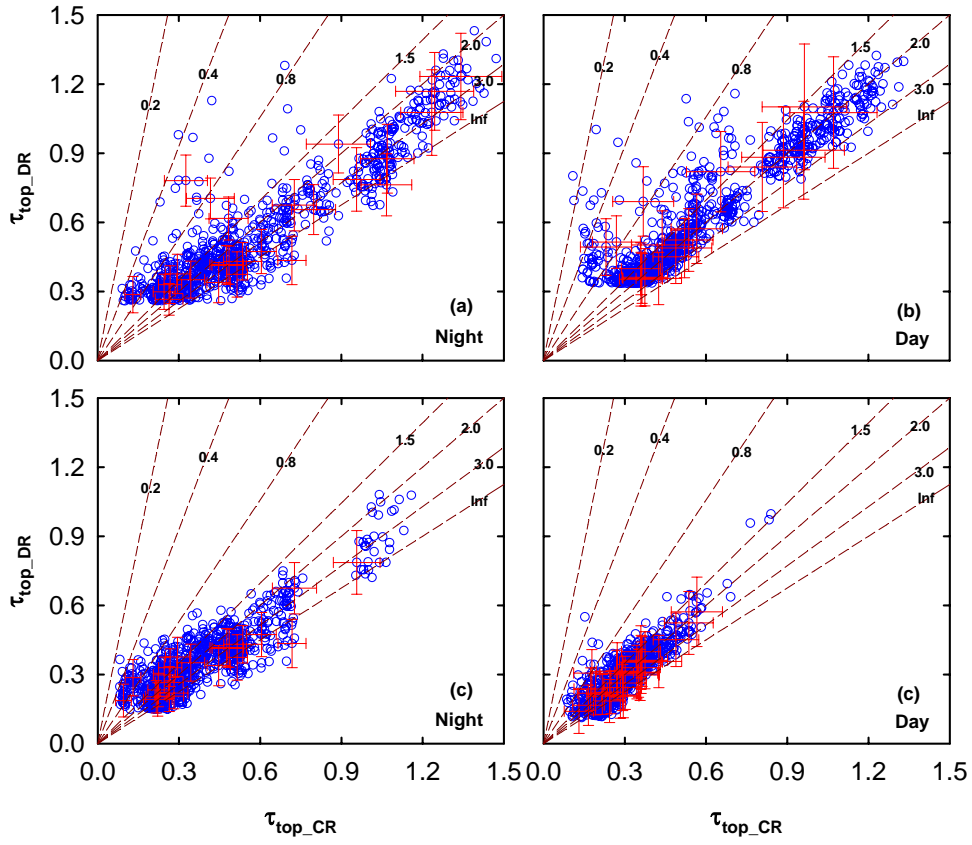


3

4

1 **Figure 4**

2



3

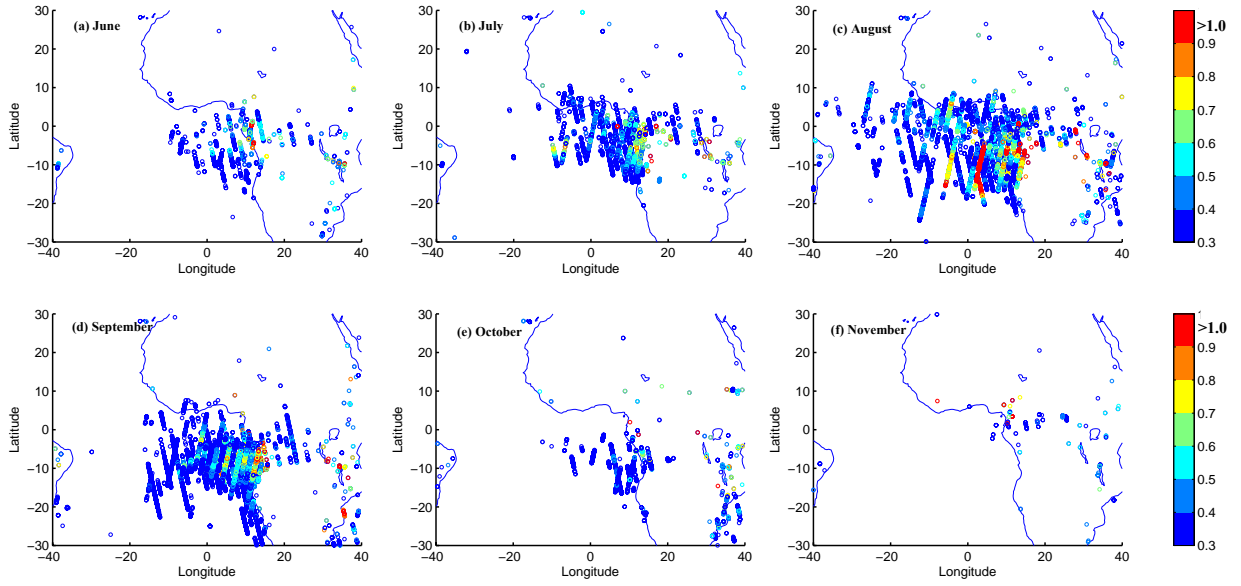
4

5

1 **Figure 5**

2

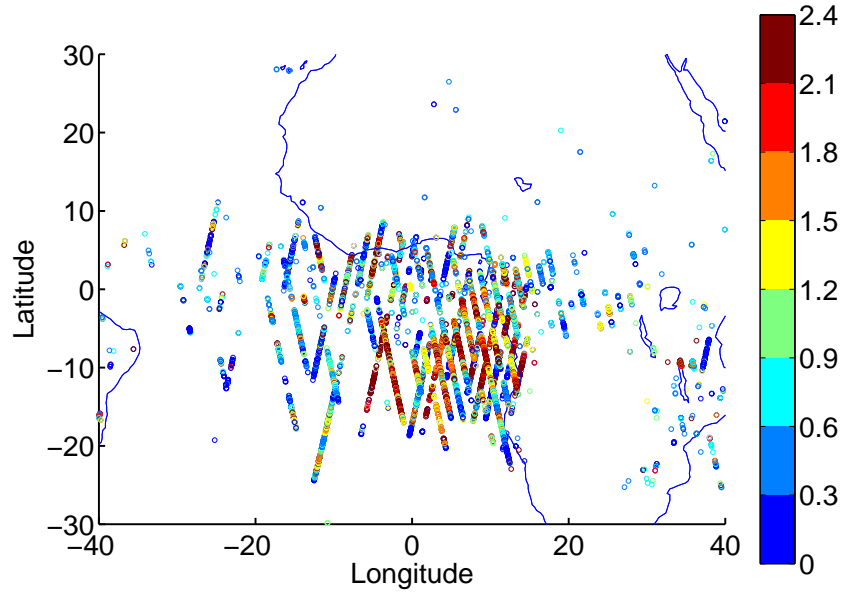
3



4

1 **Figure 6:**

2



3

4

5